DOI:10.1209/0295-5075/110/36001

Published as Europhys. Lett. **110**:36001, (2015)

Direct observation of size scaling and elastic interaction between nano-scale defects in collision cascades

X. Yi[1,2], A.E. Sand[3], D.R. Mason*[2], M.A. Kirk[4], S.G. Roberts[1,2], K. Nordlund[3], and S.L. Dudarev[2,1]

[1]Department of Materials, University of Oxford, Parks Road, Oxford, OX1 3PH, United Kingdom
[2]CCFE, Culham Centre for Fusion Energy, Abingdon, Oxfordshire OX14 3DB, United Kingdom
[3]Department of Physics, University of Helsinki, P. O. Box 43, FI-00014, Helsinki, Finland
[4]Nuclear Engineering Division, Argonne National Laboratory, Argonne, Illinois 60439, USA

May 18, 2015

Abstract

Using *in-situ* transmission electron microscopy, we have directly observed nano-scale defects formed in ultra-high purity tungsten by low-dose high energy self-ion irradiation at 30K. At cryogenic temperature lattice defects have reduced mobility, so these microscope observations offer a window on the initial, primary damage caused by individual collision cascade events. Electron microscope images provide direct evidence for a power-law size distribution of nano-scale defects formed in high-energy cascades, with an upper size limit independent of the incident ion energy, as predicted by Sand *et al.* [*Eur. Phys. Lett.*, **103**:46003, (2013)]. Furthermore, the analysis of pair distribution functions of defects observed in the micrographs shows significant intra-cascade spatial correlations consistent with strong elastic interaction between the defects.

PAC 61.72.J-,61.80.Az,68.37.Lp

*daniel.mason@ccfe.ac.uk

1 Introduction

Low dose neutron irradiation and plasma exposure gives rise to major changes in mechanical and thermal properties of plasma-facing components for ITER and future generation fusion devices [1]. Tungsten, chosen as a plasma-facing material for the ITER divertor thanks to its high-temperature strength and high thermal conductivity [2, 3], is expected to be significantly affected by neutrons produced from D-T fusion. In addition to transmutations [4], neutrons initiate collision cascades in which nano-scale defects are produced [5]. Collision cascades provide a source that drives microstructural evolution of materials under irradiation, resulting in the formation of complex dislocation and defect networks. The response of irradiated tungsten to mechanical deformation or temperature gradients differs significantly from that of the unirradiated material.

Owing to the difficulty of producing intense fluxes of neutrons with a fusion energy spectrum, self-ion irradiation is used to simulate neutron damage, and there has been recent work investigating individual ion cascade events in tungsten both experimentally[6, 7] and theoretically[8, 9, 10, 7]. As any ion moving with over the threshold displacement energy can stochastically set in motion other ions, the structure of collision cascades is fractal in nature[11]. Furthermore, at high energies cascades branch into subcascades [12, 13]. This fractal nature suggests that defect statistics may be governed by a universal power law, evidence for which has been recently found in molecular dynamics (MD) simulations of cascades in tungsten[10].

Experimental observations at room temperature are consistent with primary damage predicted by MD and evolved with Object Kinetic Monte Carlo (OKMC) simulations[7].

From the primary damage state at 10ns after a cascade event to an observation seconds later, the timescale gap bridged by OKMC is wide. Even if physically justified and carefully calibrated, OKMC based on semi-empirical laws for defect interactions and mobilities cannot by itself validate the initial defect statistics. This problem is compounded in self-ion irradiation, where the evolution is affected by the escape of radiation induced defects to the surface: what is observed in *in-situ* TEM at room temperature is merely the remnant of immobile defects.

There is currently no experimental way to make observations of individual damage events over the nano- to milli- second timescale, but it *is* possible to observe a dramatically slowed microstructural evolution using self-ion irradiation combined with *in-situ* transmission electron microscopy (TEM) at cryogenic temperature. In this study we observe defects formed in 150keV and 400keV W^+ ion cascades in ultra-high-purity tungsten foils at 30K. At this temperature isolated clusters of point defects, be they vacancy or interstitial in nature, are generally considered to be immobile [14].

We show that the distribution of sizes of visible defects measured experimentally and predicted by MD simulations of cascades in foils does indeed follow a power law, with 150keV tungsten ions producing defect distributions with an

exponent in good agreement with the foil MD simulations. We show further that 400keV tungsten ions show a slightly lower exponent in agreement with bulk MD simulations[10]. We also examine the defect pair correlation function and demonstrate that the visible defects are not distributed homogeneously in space, but rather show significant correlation between their positions. An estimate for the elastic energy of interaction between nano-scale dislocation loops of such correlations shows that for loops with diameter $d > 4$nm this energy typically exceeds 1 eV. Our observations also show there exists a maximum defect size, of order 700 point defects. We attribute the occurrence of a maximum defect size to sub-cascade branching.

2 Experimental observations

Ultra-high-purity tungsten sheets (typically W $>$ 99.996 wt%) supplied by Plansee Gruppe were used in this study. 3 mm discs were mechanically thinned to around 100 μm and annealed in vacuum at 1673 K for 20 hours. The heat treatment produced a $\{100\}\langle 011\rangle$ texture, with average grain size exceeding 10 μm. Grain boundaries and residual dislocations are therefore not expected to significantly influence radiation defect production or evolution. Finally the samples were twin-jet electropolished close to 273K using 0.5 wt% NaOH aqueous solution at an average perforation rate of 150 nm/s. Regions selected for analysis were $\sim$100 nm thick, and the micrographs free of thickness contours, so thickness variation effects are not expected. Irradiations were performed *in situ* on the IVEM-Tandem Facility at Argonne National Laboratory, with 150 keV and 400 keV W^+ ions at 30 K respectively, up to 1.25×10^{16} $W^+\mathrm{m}^{-2}$ at around 15° off the zone axis of (001) grains. This is below the fluence for cascade overlap[6], so features we see in the micrographs can be attributed to individual cascade events. Damage profiles calculated using SRIM2013 [15] monolayer damage calculation with $E_d = 55.3$eV[7] suggest that the peak damage for 150keV ions is 0.014dpa at 10nm depth; for 400keV ions it is 0.018dpa at 16nm depth. Both ion energies are expected to produce cascades contained within the foil. Weak-beam dark-field conditions ($\mathbf{g} = 200$, $\sim 3.8\mathbf{g}$) were selected for imaging defects. Image simulations [16] show that size of an image reflects the true defect size under imaging conditions characterized by an excitation error of s $\sim$0.12 nm^{-1}. At this defect size and with these imaging conditions, loops appear as single spots and do not show a 'coffee-bean' double-lobe image. Figures 1 and 2 show micrographs captured *in situ* and the final damage state.

3 Simulation methods

Molecular dynamics simulations of collision cascades resulting from self-ion irradiation in W foils were performed with the PARCAS code [17, 18, 19]. Tungsten atoms with 150 keV kinetic energy were initiated in randomly selected positions above a (014) surface, with incident angle randomly chosen within a 10° cone

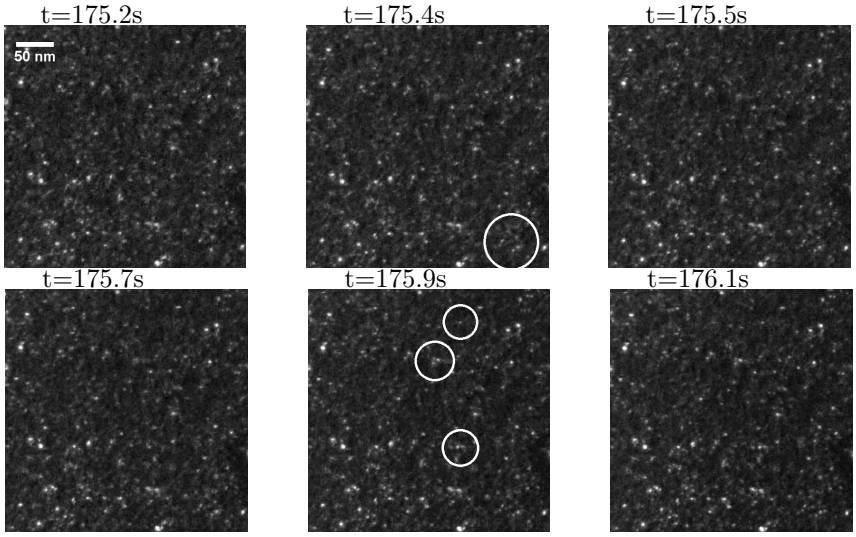

Figure 1: A sequence of snapshots taken over 1s irradiation ,(1.11 to $1.13\times10^{16}W^{+}/m^{2}$), with 400keV ions showing the space- and time- correlated appearance of nano-scale defects. Contrary to the case in iron, where the defects produced at low fluence are very small[5], individual cascade events in tungsten produce correlated clusters of defects up to 9nm diameter, which appear at full brightness in a single frame and then do not subsequently evolve.

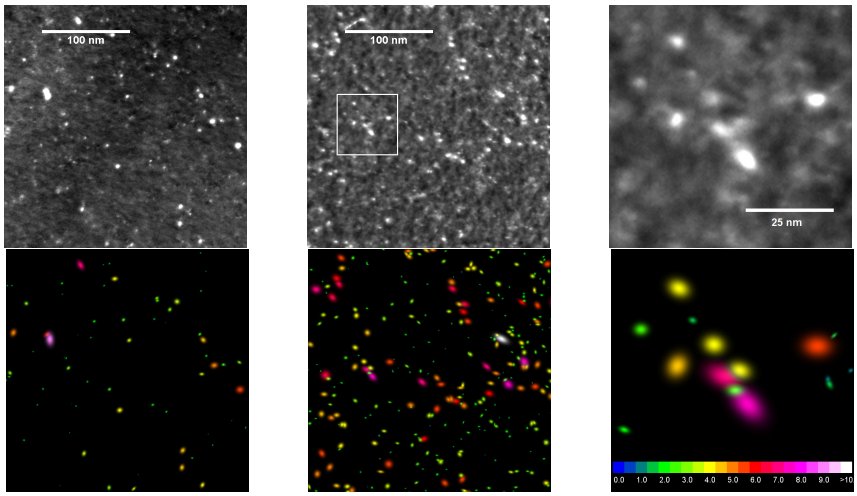

Figure 2: Defect clusters produced in collision cascades of tungsten. Top: Weak-beam dark-field imaging ($\mathbf{g} = 200$, $\sim 3.8\mathbf{g}$) of defect clusters in (left, centre) 150 keV, 400 keV W^+ ion irradiated samples, at a fluence of $1.25 \times 10^{16} W^+ m^{-2}$ at 30 K. Top right: an enlarged view showing spatially correlated defects. Bottom: computer generated interpretations of the position and size of the defects in the images above. Defects are coloured by maximum diameter, with the scale (in nm) in the coloured bar.

oriented 15° from the surface normal. A simulation box of 48×48×65 nm was used, initially at 0K, with open boundaries at top and bottom surfaces and periodic boundaries in the transverse directions centred on the impact site. A modified EAM potential [23] was used, with the repulsive part given by the universal ZBL potential [15, 24]. Electronic stopping was included for atoms with kinetic energies above 10 eV [10, 25], and atoms on the periodic borders were kept at 0K with a thermostat[20]. Counting and identification of defects was performed by an automated Wigner-Seitz method [10]. The simulation time (50ps) was sufficient for the final defects to be internally stable, and would require thermal migration for further recombination to occur.

4 Results

The size of the defects and their relative positions were extracted from experimental micrographs using an automated procedure detailed below. We were not able to confirm the nature or Burgers vector of the loops with the stage cooled to 30K. Previous studies over 273K indicated predominantly $\frac{1}{2}\langle 111\rangle$ vacancy-type loops[6, 7]. Vacancy clusters and voids would be invisible in these imaging conditions. For comparison to MD simulation results we therefore assume that each spot is formed by a circular $\frac{1}{2}\langle 111\rangle$ Burgers vector dislocation loop with diameter d, containing a number of point defects $N = \pi\sqrt{3}\,(d/(2a_0))^2$, where $a_0 = 0.3165$nm is the lattice parameter of tungsten. Measured and simulated defect size distributions were collected as histograms with varying width bins (fig. 3).

Over the loop size range $N = 50 - 500$ point defects, corresponding to loop diameters 2-6nm in the micrographs, the observed defect size frequency from 150 keV ions is fitted to a power law $f \sim A/N^S$ with $A = 2.7 \pm 1.4$ and $S = 1.8 \pm 0.1$. This is in good agreement with the distribution derived from 150keV foil simulations, where $A = 18 \pm 7$ and $S = 1.85 \pm 0.09$. 400keV ions produce a defect size distribution with $A = 3.4 \pm 2.3$ and $S = 1.6 \pm 0.2$. This can be compared to the frequency distribution with $A = 7.5 \pm 1.5$ and $S = 1.63 \pm 0.07$ found in MD simulations of cascades occurring in the bulk [10]. The power laws were fitted using linear regression, and all have an F-test significance < 0.005 and R^2 coefficient > 0.95.

Lower energy, 30 keV foil irradiation simulations show that most impacts result in heat spikes at very shallow depths, causing liquid-like cascade cores to erupt through the surface. This produces considerable sputtering, as well as viscous flow of the liquid atoms onto the surface [26], resulting in the formation of near-surface vacancy-rich zones. Such depleted zones are seen in field ion microscope observations [27], and are well reproduced by MD simulations [28]. Such cascades produce only a few small interstitial defects, biassing the size distribution to smaller defects. The agreement between 400 keV experimental observations and bulk MD simulations suggests that surface effects are not predominant in 400 keV ion irradiation. Ions penetrating deeper give rise to heat spikes contained in the bulk of the material, resulting in damage which is

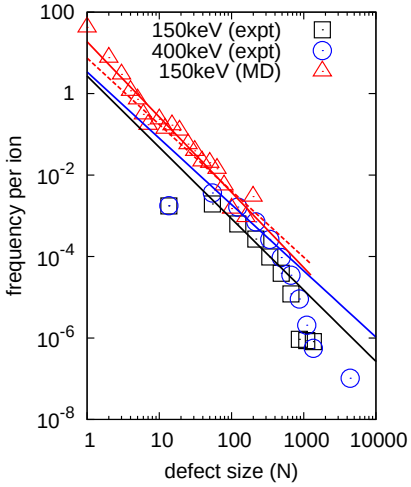

Figure 3: Histogram of defect size (N) for both experiments and MD simulations. Loops smaller than 1.5nm were difficult to distinguish from the background image intensity fluctuations; the smallest size experimental bin is the accumulated frequency for diameter $d < 1.5$nm. The dashed line shows the cluster power law found for 150 keV cascades in bulk tungsten [10]. The histograms are normalized so that the area under the curves matches the total number of defects counted.

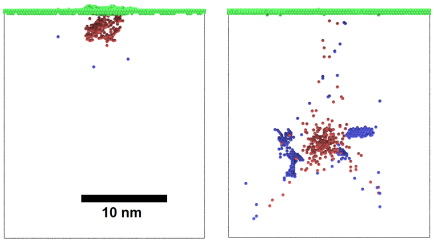

Figure 4: Typical final state configurations of (left) 30keV and (right) 150keV collision cascades in tungsten foil simulated using MD. Red spheres denote vacant lattice sites, blue spheres are self-interstitials and green are surface atoms.

statistically similar to bulk damage, with roughly equal numbers of interstitials and vacancies, and larger dislocation loops. Figure 4 shows the results of typical cascades from a 30 keV and 150 keV W ion. While only 5% of cascades from 30 keV ions resulted in a heat spike contained beneath the surface, this proportion was 50% for 150keV ions.

For loops containing more than $N = 700$ defects, there is a deviation from linearity on the log-log plot. This deviation is significant as it indicates an upper limit to the size of defects generated in the cascades. Such a limit must exist, as it is impossible for a finite energy incident ion to generate arbitrarily large dislocation loops.

No loops larger than 10nm in diameter ($N = 1300$) were observed in the 150keV irradiation experiments, and only one loop over 10nm in diameter formed during 400keV irradiation. It is not unlikely that this single very large loop was generated by the coalescence of other loops. The upper limit of the size distribution is similar for both incident ion energies, and the deviation from a power-law occurs at the same point. In our case, the likely reason for the low number of very large defects is the branching of cascades into sub-cascades above a certain threshold cascade energy, which for tungsten is close to 150 keV [10, 13].

The 150keV ion irradiations produced on average 0.27 visible loops per incident ion. This can be directly compared to 0.03 visible loops per ion in UHP W at 300K[7], indicating that at room temperature 90% of loops are sufficiently mobile to be lost to the surface or annihilate each other. The average loop diameter at 30K is 2.6nm ($N = 90$), compared to 2.0nm at room temperature, owing to the preferential annihilation of large loops[7]. The 400keV self-ion irradiation experiments produced 0.55 visible loops per incident ion, with average diameter $d = 2.9$nm ($N = 110$).

The number of visible (over 1.5nm) defects per cascade predicted by MD is greater than that seen in experiment; the foil simulations expected to produce 1.1 defects per ion if the power law is extended to $N = 700$. On the one hand, this is not surprising given the variability associated with the choice of interatomic potentials [8, 25]. On the other hand, the short time scale of MD simulations means that even mobile defects have little time to migrate and an-

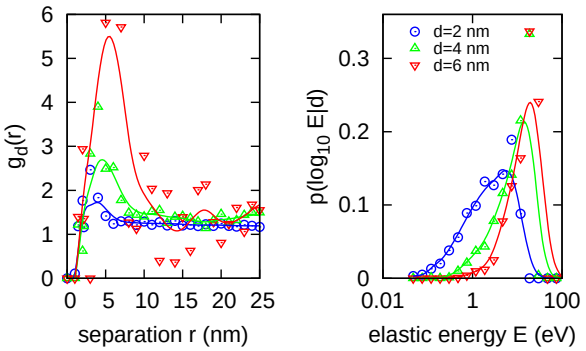

Figure 5: Analysis of spatial correlations of defect clusters obtained from micrographs of 400 keV W^+ irradiated tungsten at 30 K. (Left) The radial pair distribution function $g_d(r)$ is plotted against the separation distance r for defects with diameters over 2,4,6 nm. The solid lines are to guide the eye.(Right) The probability of finding a characteristic elastic energy, for a given observed loop diameter greater than d, computed from the size and estimated separation of the loops (see text).

nihilate, or reach the surface. The total number of defects found in a cascade simulation represents an upper bound to the possible number of surviving defects observed on experimental time scales. A further apparent feature of Fig. 3 is that the experimental distribution extends to significantly larger sizes than the distribution generated by MD. This unusual and interesting aspect of comparison between simulations and observations highlights the difference between sampling in the two cases. We analysed 50 MD cascades, whereas the 150keV experiment comprised 10000 cascades, and the 400keV experiment 20000 cascades. *In situ* experiments therefore make it possible to observe events too infrequent to find in MD simulations. The average diameter of visible loops in the simulations is $d = 2.6$nm, in agreement with experiment.

The radial distribution function $g_d(r)$, defined in eqn.A.2 as the probability of finding pairs of spots with diameters greater than d, separated by distance r is shown in fig. 5. We see a maximum correlation at $r = 4$nm, for $d = 2 - 4$nm spots in the micrographs, which is the same as the scale (4nm) of the projected radial distribution of clusters with $N \geq 30$ found in cascade simulations. Such large clusters occur infrequently in MD simulations, making a corresponding curve $g_d(r)$ for $d > 0$ less smooth. The maximum of $g_d(r)$ for $d = 0$ in the MD simulations is 9nm, decreasing to 6nm if we exclude single point defects from the analysis. The average radius of gyration r_g computed from defect cluster centres, also decreases from $r_g = 10$nm for $N \geq 1$ to $r_g = 4$nm for $N \geq 10$. This shows that in simulations, larger defects form closer together than small defect clusters or point defects.

From the relative positions of the loops in the image we can compute a typical

elastic interaction energy. While it is not possible to judge the relative depth of loops, their orientations or Burgers vectors, we can nevertheless estimate the order of magnitude. The elastic energy of interaction between two defects at distances greater than the size of the defects is

$$U_{ab} = P_{ij}^{(a)} P_{kl}^{(b)} \frac{\partial}{\partial R_j} \frac{\partial}{\partial R_l} G_{ik}(\mathbf{R}), \tag{1}$$

where $\mathbf{R}$ is the relative position of defects a and b, $P_{ij}^{(a)}$ and $P_{kl}^{(b)}$ are the defect dipole tensors, and $G_{ik}(\mathbf{R})$ is the elastic Green's function. Simplified expressions derived from this equation are given in Refs. [7, 21, 22]. For each loop in the 400keV irradiation images, the maximum value of this energy for each loop pair was computed. The result (fig. 5) illustrates that the elastic energy of interaction between pairs of loops is typically greater than 1eV for loops with diameters over 4nm. This agrees with the analysis of elasticity-mediated ordering of nano-scale dislocation loops [21, 22], and is a direct experimental confirmation of the occurrence of elastic trapping of interacting dislocation loops in cascades found in OKMC simulations[7].

5 Conclusions

In this joint experimental-theoretical work we have studied characteristics of the primary stage of radiation damage in pure tungsten foils due to self-ions. By performing *in situ* irradiations at 30K, we have restricted the mobility of defects produced in the collision cascade. To a first approximation, we can claim all defects are generated in individual cascades and become immobilised rapidly after the cascade cools, and so what we see in the TEM is very close to the final stable configuration found in (an ideal) MD simulation.

We have shown that defects generated in cascades can not be treated as isolated. Figure 5 shows that the positions of dislocation loops are correlated, and that this implies significant elastic forces acting between the loops.

We have also shown that defect size distributions from our MD simulations are in very good agreement with experiment. In particular we have demonstrated that a power-law distribution of loop sizes holds for cascades in ion-irradiated tungsten foils as well as in bulk. The spatial distributions of simulated cascades show that large dislocation loops are generated in close proximity to each other, at distances corresponding to those seen in the TEM.

These results show that the number of point defects produced per incident ion is not the only relevant metric for the subsequent evolution of the microstructure. We have shown that the distribution of loop sizes and their relative positions can be measured experimentally and are well-reproduced by MD simulation. This information is critical for determining whether elastic interactions are sufficient to bring defects together, forming an obstacle for further dislocation motion, or whether thermal fluctuations are sufficient for defects to find alternate sinks and be removed.

Acknowlegdements

The *in situ* irradiation experiments were performed at the Nuclear Engineering Division at Argonne National Laboratory, a US Department of Energy Office of Science Laboratory operated under Contract No. DE-AC02-06CH 11357 by U Chicago Argonne, LLC. We thank P. Baldo, E. Ryan and Y. Huang for help with irradiations and microscopy. XY acknowledges funding support from Culham Centre for Fusion Energy via a Research Fellowship at St. Edmund Hall, University of Oxford and from the EPSRC via the programme grant 'Materials for Fusion and Fission Power', EP/H018921/1. This work has been carried out within the framework of the EUROfusion Consortium and has received funding from the Euratom research and training programme 2014-2018 under grant agreement No 633053. The views and opinions expressed herein do not necessarily reflect those of the European Commission. To obtain further information on the data and models underlying this paper please contact PublicationsManager@ccfe.ac.uk.

References

[1] Bolt H., Barabash V., Federici G., Linke J., Loarte A., Roth J., Sato K. *J. Nucl. Mater.*, **307-311**:43, (2002).

[2] Rieth M., *et al. J. Nucl. Mater.*, **417**:463, (2011).

[3] Rieth M., *et al. J. Nucl. Mater.*, **432**:482, (2013).

[4] Gilbert, M. R., and Sublet, J.-C., *Nucl. Fusion*, **51**:043005 (2011) ; Gilbert, M. R., Dudarev, S. L., Zheng, S., Packer, L. W., and Sublet, J.-C., *Nucl. Fusion*, **52**:083019 (2012).

[5] Stoller, R. E. Primary radiation damage formation, in: *Comprehensive Nuclear Materials*, R. J. M. Konings (Ed.), Elsevier, 2012, pp 293–332.

[6] Yi, X., Jenkins, M.L., Briceno, M., Roberts, S.G., Zhou, Z., and Kirk, M.A., *Phil. Mag.*, **93**:1715, (2013).

[7] Mason, D.R., Yi, X., Kirk, M.A., and Dudarev, S.L., *J. Phys.: Condens. Matter*, **26**:375701 (2014).

[8] Fikar, J., and Schäublin, R., *J. Nucl. Mater.*,**386–288**:97 (2009).

[9] Troev, T., Nankov N., and Yoshiie T., *Nucl. Instrum. Meth. B*, **269**:566, (2011).

[10] Sand, A.E., Dudarev, S.L., and Nordlund, K., *Eur. Phys. Lett.*, **103**:46003, (2013).

[11] Moreno-Marin, J.C., Conrad, U., Urbassek, H.M., and Gras-Marti, A., *Nucl. Instrum. Meth. B*,**48**:404, (1990).

[12] Simeone, D., Luneville, L., and Serruys, Y., *Phys. Rev. E*, **82**:011122, (2010).

[13] Ryazanov, A.I., Metelkin, E.V., and Semenov, E.V., *J. Nucl. Mater.*, **386–388**:132, (2009).

[14] Amino, T., Arakawa, K., and Mori, H., *Phil. Mag. Lett*, **91**:86, (2011).

[15] Ziegler, J.F., Biersack, J.P., and Littmark, U., *The Stopping and Range of Ions in Solids*, Pergamon, (1985),

[16] Z. Zhou, M. L. Jenkins, S. L. Dudarev, A. P. Sutton, and M. A. Kirk, *Phil. Mag*, **86**:4851, (2006).

[17] K. Nordlund, *Comput. Mater. Sci.*, **3**:448, (1995).

[18] K. Nordlund, M. Ghaly, R. S. Averback, M. Caturla, T. Diaz de la Rubia, and J. Tarus, *J. Phys. Rev. B*, **57**:7556, (1998).

[19] M. Ghaly, K. Nordlund, and R. S. Averback, *Phil. Mag. A*, **79**:795, (1999).

[20] H.J.C. Berendsen, J.P.M. Postma, W.F. van Gunsteren, A. DiNola, and J.R. Haak, *J. Chem. Phys.*, **81**:3684, (1984).

[21] L.M. Brown, *Czech. J. Phys.*, **45**:893, (1995)

[22] S. L. Dudarev, M. R. Gilbert, K. Arakawa, H. Mori, Z. Yao, M. L. Jenkins, and P. M. Derlet, *Phys. Rev*, **B81**:224107 (2010); S.L. Dudarev, K. Arakawa, X. Yi, Z. Yao, M.L. Jenkins, M.R. Gilbert, P.M. Derlet, *J. Nucl. Mater.* **455**:16 (2014).

[23] Derlet, P. M., Nguyen-Manh, D., and Dudarev, S.L., *Phys. Rev. B*, **76**:054107, (2007).

[24] Björkas, C., and Nordlund, K., *Nucl. Instrum. Meth. B*, **259**:853, (2007).

[25] Sand, A. E., Nordlund, K. and Dudarev, S. L., *J. Nucl. Mater.* **455**:207, (2014); Sand, A.E. and Nordlund, K., *J. Nucl. Mater.* **456**:99, (2015).

[26] Ghaly, M. and Averback, R. S., *Phys. Rev. Lett.*, **72**:364, (1994).

[27] Wei, C.Y., Current, M.I., and Seidman, D.N., *Phil. Mag. A*, **44**:459 (1981); Current, M.I., Wei, C.Y., and Seidman, D.N., *Phil. Mag. A*, **43**:103, (1981).

[28] Zhong, Y., Nordlund, K., Ghaly, M., and Averback, R.S., *Phys. Rev. B*, **58**:2361, (1998).

[29] T. W. Ridler and S. Calvard, *IEEE Trans. Syst. Man. Cybern*, **SMC -8**:630, (1978).

6 Appendix: Analysis of micrographs

Defects visible in the micrographs were detected with a newly developed modification of Ridler and Calvard's isodata algorithm [29], proven against an extensive catalogue of measurements made by hand. Once obvious artifacts such as foil edges and screw dislocations are removed from the image, the algorithm proceeds in four stages: flattening, identifying, comparing, and counting.

The flattening stage removes long-wavelength (10s to 100s nm) variations in image intensity due to variations in the foil thickness. For each pixel i in the micrograph with intensity f_i, the average intensity $\bar{f}_i$ in a region 50x50nm is computed, excluding bright pixels over the Ridler and Calvard threshold[29]: $f_{\mathrm{thresh}} = {}^1\!/_2(\bar{f}_{\mathrm{fore}} + \bar{f}_{\mathrm{back}})$. Then the intensity of the pixel is adjusted to

$$f_i \leftarrow (f_i - 1)\left(\frac{1-\bar{f}_i}{1-\bar{f}}\right), \tag{A.1}$$

where $\bar{f}$ is a target background intensity. This flattening is repeated, averaging over a smaller 10x10nm region.

All pixels with $f_i \geq f_x \equiv {}^1\!/_2(f_{\mathrm{thresh}} + \bar{f}_{\mathrm{back}})$ are identified. A spot is defined as a contiguous region in this subset with a single maximum with intensity over f_{thresh}.

A path may exist between maxima along which the intensity remains over f_x. If this is identified, we must determine whether the spots are distinct, or merely intensity fluctuations. If the intensity on a straight line connecting two maxima drops below 70% of the linearly interpolated value, or below f_x, the maxima are treated as two spots.

With the positions and intensities of all pixels in the spot, the maximum diameter can be computed as $d = 4\lambda_g^+$, where λ_g^+ is the square root of the larger eigenvalue of the tensor $\mathbf{T} = \sum_i f_i(\vec{r}_i - \langle\vec{r}\rangle) \otimes (\vec{r}_i - \langle\vec{r}\rangle)/\sum_i f_i$.

If this procedure is applied to a reference image of unirradiated sample, spurious dim spots will be identified, corresponding to short- wavelength variations in intensity present in all TEM micrographs. The mean and standard deviation of spots in the reference image is computed, then spot in an image is accepted if its intensity passes a χ^2 test at the 5% significance level.

With the position $\vec{r}_a$ and diameter d_a computed for each spot as above, counting is straightforward. We add to the analysis the pairwise distribution $g_d(r)$, defined as

$$g_d(r) = \frac{1}{Z}\frac{1}{2}\sum_{a,b\neq a} H(d_a - d)H(d_b - d)\delta(|\vec{r}_b - \vec{r}_a| - r), \tag{A.2}$$

i.e. a count of all pairs of spots which both have diameters greater than d and are separated by distance r. $H(x)$ is the Heaviside function. The normalisation Z is chosen such that the expectation value of $g_d(r)$ is one if the spots are randomly placed, computed numerically by randomly repositioning the spots a large number of times.